The Impact of Image Reconstruction Bias on PET/CT ^{90}Y Dosimetry After Radioembolization

Katie N. Tapp[1,2], William B. Lea[1], Matthew S. Johnson[1], Mark Tann[1], James W. Fletcher[1], and Gary D. Hutchins[1]

[1]Department of Radiology and Imaging Science, Indiana University School of Medicine, Indianapolis, Indiana; and [2]School of Health Sciences, Purdue University, West Lafayette, Indiana

PET/CT imaging after radioembolization is a viable method for determining the posttreatment ^{90}Y distribution in the liver. Low true-to-random coincidence ratios in ^{90}Y PET studies limit the quantitative accuracy of these studies when reconstruction algorithms optimized for traditional PET imaging are used. This study examined these quantitative limitations and assessed the feasibility of generating radiation dosimetry maps in liver regions with high and low ^{90}Y concentrations. **Methods:** ^{90}Y PET images were collected on a PET/CT scanner and iteratively reconstructed with the vendor-supplied reconstruction algorithm. PET studies on a Jaszczak cylindric phantom were performed to determine quantitative accuracy and minimum detectable concentration (MDC). ^{90}Y and ^{18}F point-source studies were used to investigate the possible increase in detected random coincidence events due to bremsstrahlung photons. Retrospective quantitative analyses were performed on ^{90}Y PET/CT images obtained after 65 right or left hepatic artery radioembolizations in 59 patients. Quantitative image errors were determined by comparing the measured image activity with the assayed ^{90}Y activity. PET images were converted to dose maps through convolution with voxel S values generated using MCNPX, a Monte Carlo N-particle transport code system for multiparticle and high-energy applications. Tumor and parenchyma doses and potential bias based on measurements found below the MDC were recorded. **Results:** Random coincidences were found to increase in ^{90}Y acquisitions, compared with ^{18}F acquisitions, at similar positron emission rates because of bremsstrahlung photons. Positive bias was observed in all images. Quantitative accuracy was achieved for phantom inserts above the MDC of 1 MBq/mL. The mean dose to viable tumors was 183.6 ± 156.5 Gy, with an average potential bias of 3.3 ± 6.4 Gy. The mean dose to the parenchyma was 97.1 ± 22.1 Gy, with an average potential bias of 8.9 ± 4.9 Gy. **Conclusion:** The low signal-to-noise ratio caused by low positron emission rates and high bremsstrahlung photon production resulted in a positive bias on ^{90}Y PET images reconstructed with conventional iterative algorithms. However, quantitative accuracy was good at high activity concentrations, such as those found in tumor volumes, allowing for adequate tumor ^{90}Y PET/CT dosimetry after radioembolization.

Key Words: quantitative PET/CT; ^{90}Y dosimetry; reconstruction bias

Radioembolization with ^{90}Y microspheres is an established therapy for hepatocellular carcinoma or metastases to the liver. The goal of radioembolization is to deliver a highly localized absorbed radiation dose to the tumor while keeping the dose below acceptable tolerance levels in normal surrounding tissue. That goal is achieved with ^{90}Y-laden microspheres administered via intraarterial injection into branches of the hepatic artery. Preferential tumor targeting is achieved through lesion hypervascularity and the differential blood supply for tumors relative to liver parenchyma (hepatic artery vs. portal vein) (1,2). ^{90}Y is primarily a β^{-} emitter with a maximum range in soft tissue of 11 mm, producing a highly localized radiation exposure (3).

Verification of ^{90}Y-microsphere distribution, and hence radiation dose, to tumors and the surrounding liver after radioembolization has been limited in the clinic because of the complexity of obtaining in vivo quantitative images from high-energy β^{-} emitters. Consequently, most clinical estimates of radiation dose have been based on calculations that assume a uniform distribution of ^{90}Y throughout the treated volume (2,4). This simplistic, empiric approach underestimates the radiation dose to tumors and overestimates the dose to the surrounding normal tissue when there is preferential delivery to the tumors (5).

PET/CT imaging has been introduced as a feasible method to provide ^{90}Y distribution maps by leveraging β^{+}:β^{-} pair production, which occurs in approximately 32 of every 1 million decays (6–11). Many studies have demonstrated the feasibility of using these PET images for patient-specific dosimetry (12,13).

^{90}Y is not an ideal radionuclide for PET imaging because of the low pair-production branching ratio. Additionally, the ^{90}Y maximum β^{-} energy of 2.28 MeV leads to the production of bremsstrahlung photons that meet PET detector energy acceptance requirements (14), leading to increased single-event rates. The low positron-derived signal coupled with increased single events produces an image acquisition scenario with high random-to-true coincidence ratios. Random coincidence events are commonly corrected by subtracting random events measured in a delayed time window from the prompts signal. This technique, referred to as delayed random coincidence correction (DRCC), enables both real-time and offline random corrections to be performed.

In the setting of high random-to-true coincidence ratios, DRCC can produce negative sinogram ray-sum values from the stochastic nature of radionuclide decay. These negative values are often truncated in commercial software packages before iterative reconstruction to provide concavity, leading to a known positive bias (15–17). In this study, we evaluated the magnitude of this bias in the unusual setting of very high random-to-true coincidence ratios observed in ^{90}Y PET. This study also assesses the feasibility of
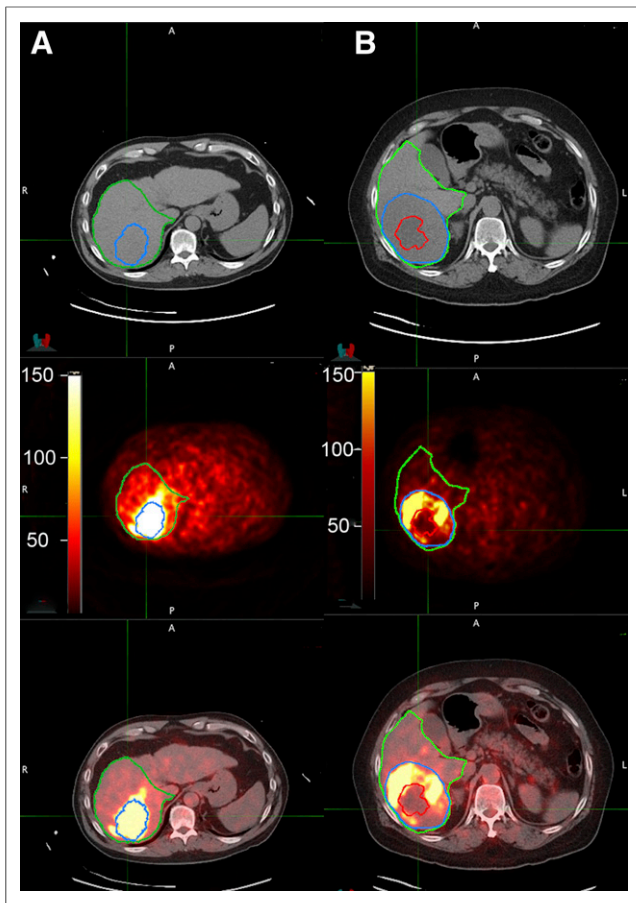
FIGURE 1. Patient PET/CT images reconstructed using TrueX following net acquisition after 3.6 GBq (A) and 3.2 GBq (B) unilobar ^{90}Y radioembolization demonstrating radionuclide quantity observed throughout FOV. Preferential lesion (blue) uptake within treated lobe (green) was observed. Minimal uptake was observed in necrotic (red) regions.

using ^{90}Y PET/CT images with observed image reconstruction bias for estimation of ^{90}Y dosimetry in tumor and treated-lobe parenchymal volumes after radioembolization.

MATERIALS AND METHODS

Image Acquisition and Reconstruction

^{90}Y PET/CT patient studies that had been acquired approximately 1 h after TheraSphere injection into the right or left hepatic artery at Indiana University Health University Hospital in Indianapolis, IN, between February 2011 and January 2013 were analyzed retrospectively. The Indiana University institutional review board approved this retrospective study, and the requirement to obtain informed consent was waived.

Data were acquired for 10 min per bed position on a Biograph 64 TrueD PET/CT scanner (Siemens Healthcare), with a 4.5-ns coincidence time window and a 435- to 650-keV energy window. The scanner consists of lutetium oxyorthosilicate (LSO) detector elements. Patient images were acquired using Siemens' net acquisition mode, which corrects for randoms in real time. Images were reconstructed using Siemens' iterative reconstruction algorithm with point-spread-function spatial recovery (TrueX), which truncates negative ray-sum values in the sinogram before image reconstruction (18). Images were reconstructed with 2 iterations and 14 subsets and had vendor-supplied DRCC, scatter, and attenuation correction applied. PET DICOM image arrays were postprocessed in IDL (Interactive Data Language; Research Systems Inc.) to apply the ^{90}Y positron branching ratio and proper decay correction.

To validate patient imaging results, images of a Jaszczak cylindric phantom containing 5 syringes with an inner diameter of 38 mm filled with 80 mL of known concentrations of ^{90}Y-Cl$_3$ solution were collected once a day for 5 d using the patient protocol. The starting total activity was 1.01 $\pm$ 0.1 GBq, calculated by subtracting residual activity measured by an Atomlab 100 (Biodex) dose calibrator from the supplier's calibration record and corrected for decay to the time of imaging. In addition to the net acquisition mode, phantom data were collected using a prompt/random acquisition mode. The prompt/random acquisition mode saves both prompt and delayed sinograms, enabling averaging or smoothing of the delayed sinogram bin values before DRCC. Given that the delayed sinogram provides an estimate of random coincidence rates, smoothing the sinogram reduces variance introduced during the DRCC (19,20). In addition to TrueX reconstruction, phantom data were reconstructed using direct inverse Fourier transform (diFT) with and without sinogram truncation to evaluate the effect of sinogram truncation.

Image Bias

Image bias was determined by comparing the administered quantity of ^{90}Y with the measured quantity of radionuclide across the image field of view (FOV). For the patient studies, the administered ^{90}Y quantity was defined as injected activity minus the estimated lung shunt fraction for image volumes that excluded most of the lungs. Manufacturer calibration records were used to determine the injected ^{90}Y activity for each patient, corrected for decay and residual activity. A 10% uncertainty was assumed for the assay of ^{90}Y quantities. The lung shunt fraction was determined by a pretreatment SPECT scan of ^{99m}Tc-macroaggregated albumin injected during the patient's planning arteriogram obtained approximately 2 wk before radioembolization. PET images with 2 bed positions contained a majority of the lung in the FOV, and therefore no subtraction was made to remove the lung activity in defining the administered FOV quantity. The administered whole-liver quantity was corrected for the lung shunt fraction in all studies.

For the phantom studies, the total radionuclide quantity measured across the entire PET FOV was compared with the total syringe activity. With IDL software, net acquisition uncorrected sinogram values were binned to create a histogram to demonstrate the distribution of positive and negative values observed after real-time DRCC.

In acquisitions with a low signal, the natural radioactivity of ^{176}Lu in the LSO crystals may produce a significant portion of the random
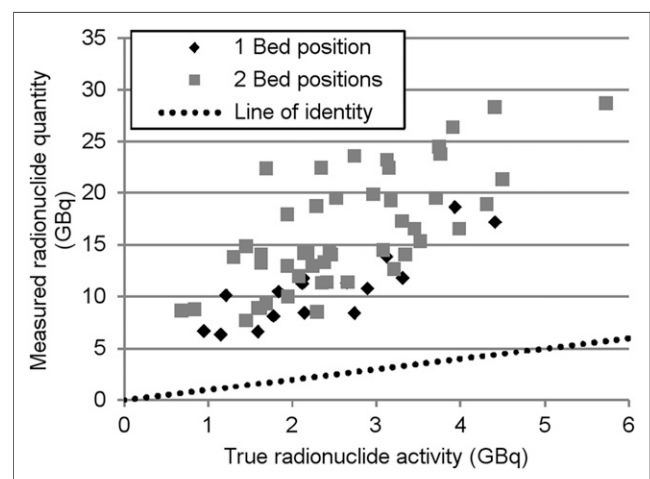

FIGURE 2. Calculated activity observed throughout FOV exceeded true radionuclide quantity in all patient PET/CT images reconstructed using TrueX after net acquisition. Larger positive bias was found on average in 2-bed-position acquisitions, which had larger FOV volumes.
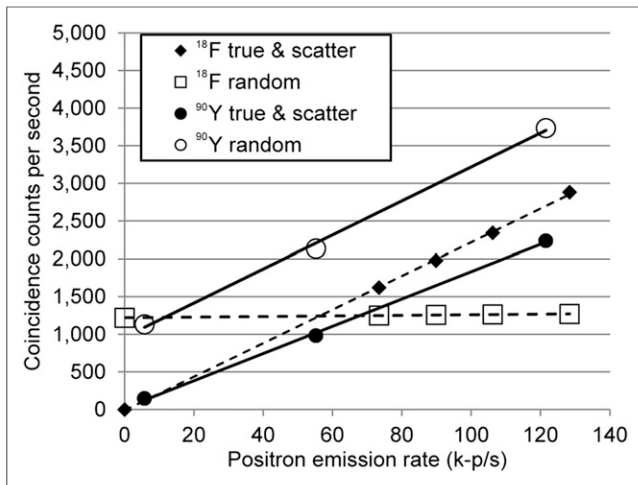
FIGURE 3. ^{18}F and ^{90}Y counting rates demonstrate increased random events in ^{90}Y acquisitions compared with ^{18}F at same positron emission rate whereas true and scatter events stay approximately the same. ^{90}Y random events were seen to increase from background acquisition, where no activity was present besides natural ^{176}Lu found in LSO crystals. ^{18}F random events were not seen to have a significant increase beyond background LSO counts because of the low activity needed to match ^{90}Y positron emission rate.

coincident events. To evaluate the proportion of the bias caused by the LSO, a cold phantom acquisition was collected 13 d after manufacturing to allow for decay.

Prompt, random, and true events were recorded from multiple acquisitions of ^{90}Y and ^{18}F point sources to evaluate the impact of bremsstrahlung photons on random-coincidence counting rates. Three acquisitions of ^{90}Y activities—3.8, 1.7, and 0.2 GBq—contained in original TheraSphere vials were collected. Additionally, 4 acquisitions were collected every half hour with a vial filled with ^{18}F. The ^{18}F activity for the first acquisition was 0.13 MBq, decay-corrected from an initial activity of 8.5 MBq as determined by the dose calibrator. An additional acquisition was collected with no activity present to determine the background counting rate.

Quantitative Accuracy and Minimum Detectable Levels

Quantitative accuracy was determined by comparing the observed syringe radionuclide quantity in the phantom images with the true activity. Measured radionuclide quantities were calculated using a region-growing tool on CT images to create volumes of interest (VOIs). Each VOI was expanded by 1 pixel length (4 mm) around its surface using MIMVista software to ensure that all activity in each syringe was measured.

Minimum detectable concentration (MDC) was determined using the Rose criterion, which bases detection limits on a minimum contrast-to-noise ratio (CNR) (21), as found in the following equation:

$$CNR = \frac{C_L - C_B}{\sigma_B}, \qquad \text{Eq. 1}$$

where C_L, C_B, and σ_B are lesion concentration, background concentration, and background noise, respectively. A contrast-to-noise ratio of 8 has been suggested for ^{90}Y PET images because of high noise (11). The MDC is then defined as:

$$MDC = 8\sigma_B + C_B. \qquad \text{Eq. 2}$$

Each phantom background SD was determined following the method described by Stute et al. (22) using the mean SD from 10 regions of interest consisting of 45 voxels placed at random at least 2 pixel

lengths apart and 3 pixel lengths from the border and syringe VOIs (11).

Absorbed Dose Maps

PET radionuclide concentration images were converted to dose maps in accordance with MIRD 17 (23). Voxel S values were constructed for the PET voxel size ($4.07 \times 4.07 \times 3$ mm) using MCNPX, a Monte Carlo N-particle transport code system for multiparticle and high-energy applications (24), using 10^8 starting β^- particles and a cutoff energy of 1 keV. Dose maps were generated by convolving the voxel S values with PET DICOM cumulative activity arrays in IDL.

Phantom syringe VOI dose measurements were used to validate dose map results through comparison with expected dose values using the clinical dosimetry equation:

$$D = \frac{50A}{M}, \qquad \text{Eq. 3}$$

where A is activity in gigabecquerels, M is mass in kilograms assuming liver tissue density, and D is dose in grays (25).

Patient Dosimetry

Image radionuclide quantities and tissue volumes were estimated from radiologist-defined contours created on associated CT images for all patient studies (Fig. 1). Only tumors larger than 1 cm were included in the study. Studies with indiscernible tumor boundaries were excluded. Tumors with large necrotic centers were contoured to differentiate between viable and nonviable tumor volumes. Healthy-parenchyma contours were constructed by removing tumor volumes from the treated lobe contours. Mean tumor doses were estimated by placing the contours on the PET dose maps.

Measured quantities are expected to be overestimated in voxels with a concentration below the MDC. The maximum potential activity from bias can be quantified by assuming that all activity in voxels below the MDC is from bias. The MIMVista upper-threshold tool set to the MDC was used to determine this maximum bias activity for each VOI. Maximum bias activity can be converted to maximum dose bias by separating the activity from measurements above and below the MDC in the clinical dosimetry equation,
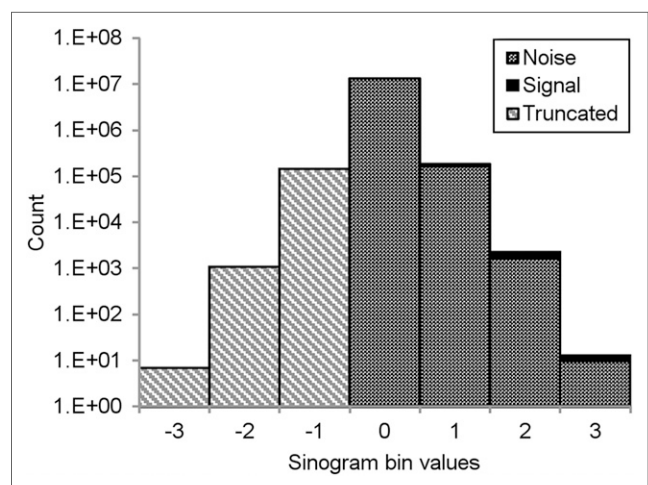

FIGURE 4. Histogram of phantom-acquisition sinogram ray-bin values after online DRCC subtraction demonstrates that significant negative bins are created in ^{90}Y PET images. Truncation of these negative values before reconstruction leaves only positive noise.

Day	True activity (MBq)	TrueX, net acquisition (MBq)	TrueX, prompt/random acquisition (MBq)	DiFT, net acquisition (MBq)	Truncated DiFT, net acquisition (MBq)
1	1,008	3,755 [273]	1,002 [−0.6]	800 [−21]	3,250 [222]
2	793	3,562 [349]	819 [3.3]	616 [−22]	3,135 [295]
3	610	3,282 [438]	628 [3.0]	446 [−27]	2,935 [381]
4	475	3,140 [561]	529 [11]	318 [−33]	2,777 [485]
5	362	3,067 [747]	454 [25]	244 [−33]	2,752 [660]
13	34.7	2,596 [7,381]	147 [324]	−46 [−233]	2,362 [6,707]

DiFT = direct inverse Fourier transform.
Data in brackets are percentage error.

$$D = \frac{50A_+}{M} + \frac{50A_-}{M}. \qquad \text{Eq. 4}$$

In this equation, A_+ represents the activity measured above the MDC, A_- is activity measured below the MDC, and M is the whole volume mass. The second term, with the activity measured below the MDC, represents the potential dose bias.

Statistical Analysis

Data are expressed as mean ± SD. Phantom VOIs with a concentration above and below the MDC quantitative accuracy measurements were compared with the nonparametric Wilcoxon rank sum test since the continuous measurements were not normally distributed.

RESULTS

Image Reconstruction Bias in Patient Studies

Sixty-five PET/CT acquisitions after right ($n = 48$) and left ($n = 17$) hepatic artery radioembolization from 59 patients were included in the analysis, with 16 and 49 having 1 and 2 bed positions, respectively. The mean injected activity was 2.6 GBq, with a range of 0.7–5.7 GBq. The mean lung shunt fraction was 5.3% ± 2.6% and 7.6% ± 4.0% for 1 and 2 bed positions, respectively. Diffuse background activity was observed in all patient PET images (Fig. 1). In the total-image FOV, the measured radionuclide quantities exceeded the administered radionuclide quantity by an average of 8.4 and 13.5 GBq for 1 and 2 bed positions, respectively, when TrueX was

used after net acquisition (Fig. 2). The mean measured quantity in whole-liver VOIs was 0.6 ± 0.6 GBq greater than expected.

Phantom Image Reconstruction Bias

Bremsstrahlung photons increased the ^{90}Y random coincidence event rates compared with ^{18}F for equivalent positron emission rates, whereas true-plus-scatter counting rates were found to be similar (Fig. 3). At 3.8 GBq, ^{90}Y provided a 3.06-fold increase in random events compared with background coincidence rates observed with no activity present. However, interpolation of the ^{18}F random-event-rate results showed that ^{18}F at the same emission rate of 121,500
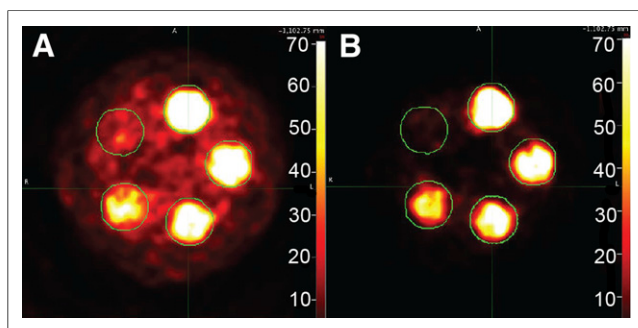

FIGURE 5. Reconstructed images from net (A) and prompt/random (B) acquisitions of phantom. In each case, random coincidence corrections were applied. Images demonstrate that diffuse bias in background decreases after smoothing of random sinogram before DRCC in prompt/random acquisition mode.
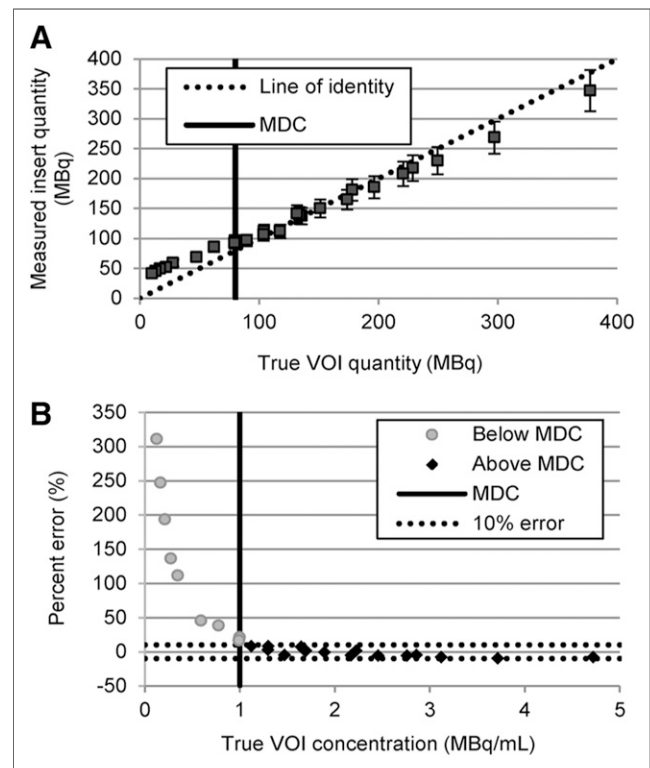

FIGURE 6. Phantom-insert VOI measurements from images reconstructed using TrueX after net acquisition were found to have accuracy within 10% at concentrations above MDC of 1 MBq/mL (A), with percentage error increasing to above 10% for VOI with concentrations below MDC (B).

TABLE 2
Phantom Image Activity and Dose Estimated from TrueX Reconstruction of Data Collected Using Net Acquisition Mode

Syringe concentration (MBq/mL)	Day/syringe	True activity (MBq)	VOI activity (MBq)	Expected dose (Gy)	Calculated dose (Gy)	Dose error (%)
4.72	1/1	378	347	147	135	−8.4
3.71	2/1	297	268	113	102	−9.9
3.12	1/2	250	230	99	91	−8.1
2.86	3/1	229	217	88	86	−2.3
2.76	1/3	221	208	85	80	−3.2
2.45	2/2	196	185	74	70	−6.1
2.22	4/1	178	181	72	71	−0.8
2.17	2/3	174	164	66	62	−6.0
1.89	3/2	151	150	59	60	1.9
1.69	5/1	136	137	57	57	1.0
1.67	3/3	134	138	51	54	6.5
1.65	1/4	132	144	51	56	9.4
1.47	4/2	118	112	49	49	0.9
1.30	4/3	104	112	41	43	4.0
1.30	2/4	104	107	39	41	3.2
1.12	5/2	90	97	38	41	8.3
0.99	3/4	80	96	31	39	24.8
0.99	5/3	79	92	32	37	16.5
0.78	4/4	62	86	24	34	38.7
0.59	5/4	47	69	19	28	45.8
0.35	1/5	28	59	11	24	113.1
0.27	2/5	22	52	9.1	22	138.5
0.21	3/5	17	49	6.6	20	206.9
0.16	4/5	13	45	5.4	19	244.4
0.12	5/5	10	41	4.2	17	317.9

positrons per second (0.13 MBq of ^{18}F) produced random events at only 1.03 times background.

A histogram of detected ray-sum values, after net acquisition from the highest-activity phantom, demonstrated that 46.8% of nonzero values were negative (Fig. 4). Phantom net acquisition images with real-time DRCC subtraction had radionuclide quantities measured across the FOV that exceeded the total radionuclide quantity placed in the syringes, with percentage errors in the range of 273%–747% observed during the first 5 d of imaging (Table 1; Fig. 5A). The range dropped to −0.6%–26% when the delayed window was smoothed with the prompt/random acquisition, with the 3 highest-activity images having less than 10% error (Fig. 5B).

Additionally, positive bias was not observed in any images after net acquisition using diFT reconstruction. Positive bias was observed after this reconstruction when the net acquisition sinogram was truncated before reconstruction.

Quantitative Accuracy

The ^{90}Y MDC for the phantom study was found to be 1 MBq/mL. Quantity and dose measurements from the 16 syringes containing activity above the MDC matched expected values within 10% (Fig. 6; Table 2). VOI measurements in the 9 syringes with concentrations below the MDC were higher than expected. The pos-

itive bias observed in the syringe VOIs with concentrations below the MDC produced absolute errors that were greater than the absolute errors observed for VOI measurements in syringes with concentrations above the MDC ($P < 0.0003$).

Patient Results

From the 65 studies, the treated-lobe concentration based on expected liver activity assuming a uniform distribution was greater than the MDC (range, 1.03–3.64 MBq/mL). However, visual observation confirmed that ^{90}Y was heterogeneously distributed, resulting in an average treated-lobe volume with ^{90}Y concentration below the MDC of 277.4 ± 204.1 mL, with a range of 25.9 to 1,353.7 mL. Because of increased uptake in the tumor, most of this volume was found in the parenchyma, with an average of 247.8 ± 149.0 mL, corresponding to an average of 27.3% ± 16.9% of the total parenchyma (Fig. 7A). The mean total quantity measured in the treated-parenchyma volume with ^{90}Y concentrations below the MDC was 170.1 ± 99.4 MBq. This resulted in a mean potential bias of 8.9 ± 4.9 Gy, compared with the mean calculated dose of 97.1 ± 22.1 Gy (Fig. 7B).

The volume with ^{90}Y concentration below the MDC in the 115 identified tumors was 16.7 ± 75.8 mL, corresponding to 12.2% ± 23.1% of lesion volume, resulting in an average total measured quantity of 15.8 ± 55.3 MBq. This resulted in a mean potential bias
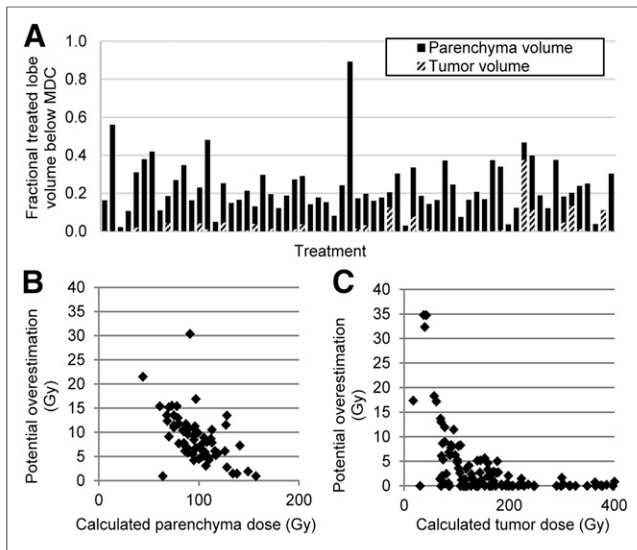
FIGURE 7. Heterogeneous ^{90}Y microsphere distribution led to 31.3% ± 25.7% (mean ± SD) of treated lobe volume having measured concentration below MDC. (A) Because of preferential delivery to tumor, volume below MDC was larger in parenchyma in 63 of 65 studies. (B and C) Quantity measured in these volumes led to greater than 10% potential dose bias in parenchyma for 42% (27/65) of studies (B) and 9% (10/115) of tumors (C). Dose maps showed poor preferential ^{90}Y deposition, with calculated dose being less than 100 Gy in all 10 tumors that had greater than 10% potential dose bias.

of 3.3 ± 6.4 Gy, compared with the mean measured viable tumor dose of 183.6 ± 156.5 Gy (Fig. 7C).

DISCUSSION

A large positive bias in the total radionuclide quantity in patient ^{90}Y PET/CT images was observed when negative sinogram values were truncated before iterative reconstruction. Based on the phantom study, the positive bias was found to be restricted to regions where ^{90}Y concentrations fell below the MDC. The study demonstrated that the ^{90}Y PET/CT–measured radionuclide concentration was quantitatively accurate, even in the presence of significant positive bias within the image volume, in areas found to contain ^{90}Y concentrations above the MDC.

In the setting of very low coincidence-detection rates and high single-event rates (as observed in our ^{90}Y PET studies), a large number of the sinogram elements are negative after online DRCC because of the stochastic nature of the random coincidence events detected in both the prompt and the delayed coincidence windows. Truncation of negative values leaves only the positive values of the background noise distribution in the sinogram. Reconstruction of sinograms in which negative values have been truncated artificially generates radionuclide concentrations in regions of the image that have low radionuclide concentrations while having minimal impact on the reconstructed value in regions of the image with high radionuclide concentrations. Our phantom studies with and without sinogram truncation when the direct inversion Fourier transformation reconstruction algorithm is used provide a nice demonstration of the impact of truncation in PET studies with a low coincidence rate and a high single-event rate. Our study also demonstrated that smoothing the delayed-window random coincidence rates before subtraction reduced the observed bias. This type of positive bias is well documented for PET images reconstructed

using iterative algorithms with truncated sinograms in the setting of low signal-to-noise ratios (15–17).

Past studies have suggested that at a low signal, natural radioactive decay of [176]Lu, found in LSO PET crystals, can cause most of the random events leading to the positive bias (11). However, the experimental findings from the ^{90}Y point-source study showed an increase in random coincidences for the ^{90}Y source as compared with background or an equivalent rate of positron emission from an ^{18}F source. The increase is due to bremsstrahlung photons, produced by the [90]Y 2.28-MeV maximum-energy β⁻ particle, contributing a significant rise in random events. Truncation of negative sinogram values produced by the correction for these random events creates a mean excess of 8.4 GBq across the FOV for a 1-bed-position study. In comparison, the 1-bed-position study of the cold phantom produced an excess of 2.6 GBq. Therefore, the biased background signal observed in regions below the MDC is due to both bremsstrahlung and natural radioactivity in LSO crystals.

Even with the large positive bias observed when the radionuclide levels throughout the imaging FOV were quantified, the phantom study demonstrated quantitative accuracy for concentrations above the MDC, confirming previous literature findings that ^{90}Y PET images are accurate at high concentrations (6,11). Through use of voxel MIRD methodology, these images also provided accurate dose results for each of these VOIs. As expected, bias was observed in VOIs with concentrations less than the MDC, resulting in an overestimation of both radionuclide concentration and radiation dose.

Overestimation of the quantity of ^{90}Y in the liver volume was evident in all 65 patient studies, even when one considers a 10% uncertainty in the original ^{90}Y assay. Positive bias is expected to have influenced the dose results for all patients in this study because of areas with a concentration below the MDC of 1 MBq. However, because of preferential uptake of ^{90}Y microspheres in tumors, most tumors had a small volume with a concentration below the MDC. This favorably results in minimal positive bias within the tumor volume. Thus, the potential for error in ^{90}Y concentration estimates from the bias in most tumors was relatively small. Ninety-one percent (105/115) of identified tumors had a potential bias of less than 10 Gy. The 10 tumors that had a potential bias greater than 10 Gy all had calculated doses of less than 100 Gy because of low ^{90}Y deposition. In these 10 tumors, the calculated dose is still known to be less than 100 Gy because the bias was positive.

Unfortunately, the nonuniform distribution caused a large portion of the parenchymal volume to be below the MDC. The result was an average potential bias of 8.9 Gy, with 40% (26/65) of studies having a potential bias greater than 10 Gy because of the image reconstruction bias. This observation demonstrates that great care must be taken in trying to assess radiation dose to normal liver parenchyma based on ^{90}Y PET images when reconstruction algorithms that truncate negative sinogram values are used.

CONCLUSION

Because of low positron signal compared with noise from LSO and bremsstrahlung photons, a large number of sinogram ray-sum values are negative after DRCC subtraction, leading to position bias when truncated in iterative reconstruction algorithms. Even in the presence of this positive bias, quantitative accuracy was good in areas where the concentration was above the MDC, enabling accurate estimation of ^{90}Y PET/CT tumor dosimetry after radioembolization. A large positive bias was observed in regions with low ^{90}Y concentrations, such as are found in large areas of the

parenchyma in many studies, when sinogram truncation with iterative reconstruction is used. Therefore, care must be taken in the selection of a reconstruction algorithm for estimation of radionuclide concentration and dosimetry in low-uptake regions of the image such as the liver parenchyma.

DISCLOSURE

REFERENCES

1. Lewandowski RJ, Sato KT, Atassi B, et al. Radioembolization with 90Y microspheres: angiographic and technical considerations. *Cardiovasc Intervent Radiol.* 2007;30:571–592.
2. Dancey JE, Sphepherd FA, Paul K, et al. Treatment of nonresectable hepatocellular carcinoma with intrahepatic 90Y-microspheres. *J Nucl Med.* 2000;41:1673–1681.
3. Sarfaraz M, Kennedy AS, Coa ZJ, et al. Physical aspects of yttrium-90 microsphere therapy for nonresectable hepatic tumors. *Med Phys.* 2003;30:199–203.
4. Salem R, Thurston KG. Radioembolization with 90yttrium microspheres: a state-of-the-art brachytherapy for primary and secondary liver malignancies. Part 1: technical and methodologic considerations. *J Vasc Interv Radiol.* 2006;17:1251–1278.
5. Gulec SA, Mesoloras G, Stabin M. Dosimetric techniques in 90Y-microsphere therapy of liver cancer: the MIRD equations for dose calculations. *J Nucl Med.* 2006;47:1209–1211.
6. Gates VL, Esmail AA, Marshall K, Spies S, Salem R. Internal pair production of 90Y permits hepatic localization of microspheres using routine PET: proof of concept. *J Nucl Med.* 2011;52:72–76.
7. Lhommel R, Goffette P, Van den Eynde M, et al. Yttrium-90 TOF PET scan demonstrates high-resolution biodistribution after liver SIRT. *Eur J Nucl Med Mol Imaging.* 2009;36:1696.
8. Willowson K, Forwood N, Jakoby BW, Smith AM, Bailey DL. Quantitative 90Y image reconstruction in PET. *Med Phys.* 2012;39:7153–7159.
9. Kao YH, Tan EH, Ng CE, Goh SW. Yttrium-90 time-of-flight PET/CT is superior to bremsstrahlung SPECT/CT for postradioembolization imaging of microsphere biodistribution. *Clin Nucl Med.* 2011;36:e186–e187.
10. Bagni O, D'Arienzo M, Chiaramida P, et al. 90Y-PET for the assessment of microsphere biodistribution after selective internal radiotherapy. *Nucl Med Commun.* 2012;33:198–204.
11. Carlier T, Eugène T, Bodet-Milin CB, et al. Assessment of acquisition protocols for routine imaging of Y-90 using PET/CT. *EJNMMI Res.* 2013;3:11.
12. Lhommel R, van Elmbt L, Goffette P, et al. Feasibility of 90Y TOF PET-based dosimetry in liver metastasis therapy using SIR-Spheres. *Eur J Nucl Med Mol Imaging.* 2010;37:1654–1662.
13. D'Arienzo M, Chiaramida P, Chiacchiararelli L, et al. 90Y PET-based dosimetry after selective internal radiotherapy treatments. *Nucl Med Commun.* 2012;33:633–640.
14. Selwyn RG, Nickles BR, Thomadsen BR, DeWerd LA, Micka JA. A new internal pair production branching ratio of 90Y: the development of a non-destructive assay for 90Y and 90Sr. *Appl Radiat Isot.* 2007;65:318–327.
15. Ahn S, Fessler JA. Emission image reconstruction for randoms-precorrected PET allowing negative sinogram values. *IEEE Trans Med Imaging.* 2004;23:591–601.
16. Rahmim A, Cheng JC, Blinder S, Camborde ML, Sossi V. Statistical dynamic image reconstruction in state-of-the-art high resolution PET. *Phys Med Biol.* 2005;50:4887–4912.
17. Li Q, Leahy RM. Statistical modeling and reconstruction of randoms precorrected PET data. *IEEE Trans Med Imaging.* 2006;25:1565–1572.
18. Casey ME. *Point Spread Function Reconstruction in PET.* Malvern, PA: Siemens Medical Solutions; 2007.
19. Casey ME, Hoffman EJ. Quantitation in positron emission computed tomography: 7—a technique to reduce noise in accidental coincidence measurements and coincidence efficiency calibration. *J Comput Assist Tomogr.* 1986;10:845–850.
20. Brasse D, Kinahan PE, Lartizien C, et al. Correction methods for random coincidences in fully 3D whole-body PET: impact on data and image quality. *J Nucl Med.* 2005;46:859–867.
21. Bao Q, Chatziioannou AF. Estimation of the minimum detectable activity of preclinical PET imaging systems with an analytical method. *Med Phys.* 2010;37:6070–6083.
22. Stute S, Carlier T, Cristina K, et al. Monte Carlo simulations of clinical PET and SPECT scans: impact of the input data on the simulated images. *Phys Med Biol.* 2011;56:6441–6457.
23. Bolch WE, Bouchet LG, Robertson JS, et al.; Medical Internal Radiation Dose Committee. MIRD pamphlet no. 17: the dosimetry of nonuniform activity distributions—radionuclide S values at the voxel level. *J Nucl Med.* 1999;40(suppl):11S–36S.
24. Dieudonné A, Hobbs RF, Bolch WE, Sgouros G, Gardin I. Fine-resolution voxel S values for constructing absorbed dose distributions at variable voxel size. *J Nucl Med.* 2010;51:1600–1607.
25. Package insert: TheraSphere® yttrium-90 glass microspheres. TheraSphere website. http://www.therasphere.com/physicians-package-insert/package-insert-us.pdf. Accessed June 17, 2014.